

RESEARCH ARTICLE

[View Article Online](#)
[View Journal](#) | [View Issue](#)



Cite this: *Inorg. Chem. Front.*, 2022, 9, 6237

Plasma-assisted rhodium incorporation in nickel–iron sulfide nanosheets: enhanced catalytic activity and the Janus mechanism for overall water splitting†

Junying Li,^a Xiaodeng Wang,^{*b} Lingya Yi,^a Changxiang Fang,^a Tianhao Li,^{ID, a} Wei Sun^{*c} and Weihua Hu^{ID, *a}

NiFe catalysts show compelling oxygen evolution reaction (OER) activity in alkaline solution but their hydrogen evolution reaction (HER) activity is limited. In this work Rh was incorporated in Fe-doped Ni_3S_2 nanosheets with the assistance of hydrogen plasma to significantly enhance the HER/OER catalytic activity. The resultant catalyst, *p*-Rh/Fe- Ni_3S_2 /NF, was composed of Rh/Rh₂S₃ heterostructured clusters embedded in Fe- Ni_3S_2 nanosheets; it needs overpotentials of only 108 and 237 mV to achieve HER and OER currents of 100 mA cm⁻², respectively, and drives overall water splitting at 1.79 V with a current of 100 mA cm⁻² as a bifunctional catalyst. Post-characterization and density functional theory (DFT) calculation reveal its *operando* evolution behavior and a unique Janus catalytic mechanism for the HER and OER. For the HER, a Rh/Rh₂S₃ heterointerface with strong H₂O adsorption energy and optimal H adsorption energy is the active site; in the OER, it experiences surface transformation under *operando* conditions; an *in situ* formed Rh/Fe-doped NiOOH layer with strengthened binding of *O facilitates the rate determining step of *O formation to accelerate the OER process. Hydrogen plasma treatment not only helps partially reduce Rh to form HER-active Rh/Rh₂S₃ heterostructures but also induces rich defects/vacancies to facilitate surface reconstruction/phase transformation to form an active co-doped NiOOH phase under OER conditions. This work may shed light on the promotive role of noble metals on NiFe-based catalysts for water splitting.

Received 30th July 2022,
Accepted 5th October 2022

DOI: 10.1039/d2qi01655a
rsc.li/frontiers-inorganic

1. Introduction

Electricity-driven water splitting to hydrogen fuel is one of the promising techniques for sustainable grid-scale energy storage.¹ For high energy efficient water splitting, it is an urgent task to explore active electrocatalysts with low content/free of precious metals for its two sluggish half-reactions, namely hydrogen evolution reaction (HER) and oxygen evol-

ution reaction (OER).^{2,3} Ni/Fe based materials have been the focus of intensive research for years due to their excellent OER activity in alkaline solution.^{4,5} Most of these catalysts experience *operando* surface reconstruction and the *in situ* formed Fe-doped nickel oxyhydroxide (NiOOH) phase is the real active phase.^{6,7} The Fe atoms in these catalysts, either added on purpose or incidentally as contaminants, are found to be critical for the overall OER activity while the NiOOH provides a suitable matrix for dynamic balance.^{8,9} Despite their excellent OER activity, Ni/Fe catalysts possess low HER activity as a consequence of weak hydrogen adsorption.¹⁰ To enhance their HER activity for possible Janus/bifunctional electrocatalysis in water electrolysis, bimetal phosphides and sulfides were synthesized but their HER catalytic performance is far from satisfactory.^{11,12}

In recent years a new strategy has been emerging by introducing Pt-group metals in the form of single-atom dopants, clusters or nanoparticles into NiFe catalysts to further boost their OER while significantly improving their HER performance.^{10,13,14} For the OER, precious metal species in the high valence state were stabilized by the NiFe matrix to accelerate the O–O bond formation; the adsorption energy of multiple

^aKey Laboratory of Luminescent and Real-Time Analytical Chemistry (Southwest University), Ministry of Education, School of Materials and Energy, Southwest University, Chongqing 400715, China. E-mail: whhu@swu.edu.cn

^bChongqing Engineering Research Center of New Energy Storage Devices and Applications, Chongqing University of Arts and Sciences, Chongqing, 402160, China. E-mail: wangxd@cqwu.edu.cn

^cKey Laboratory of Laser Technology and Optoelectronic Functional Materials of Hainan Province, Key Laboratory of Functional Materials and Photoelectrochemistry of Haikou, College of Chemistry and Chemical Engineering, Hainan Normal University, Haikou 571158, China. E-mail: sunwei@hainnu.edu.cn

† Electronic supplementary information (ESI) available: DFT calculation details, SEM images, SAED, XPS, CV, LSV, TEM images, XRD patterns, and faradaic efficiency. See DOI: <https://doi.org/10.1039/d2qi01655a>

oxygen-containing intermediates was also optimized.^{15,16} For the HER, the appropriate hydrogen adsorption energy of Pt-group metal enables fast hydrogen evolution while the NiFe matrix as a co-catalyst enables fast water dissociation in alkaline solution.^{10,17,18} Although the detailed mechanism remains controversial, these encouraging works point to an intriguing direction for the rational design of bifunctional catalysts for water splitting.

Heazlewoodite (Ni_3S_2) is a naturally occurring mineral and inspires considerable research interest for water splitting due to its intrinsically high conductivity and rich yet well-controllable nanostructures.^{19,20} Its OER and HER performance were manipulated and explored *via* e.g., engineering of high-index facets, incorporation of other metallic sulfide/oxide nanoparticles, *etc.*^{19,21,22} However, their electrocatalytic performance needs improvement for practical applications.

In this work, a highly active bifunctional catalyst was reported for alkaline water electrolysis by incorporating Rh in Ni_3S_2 nanosheets on Ni foam with the assistance of hydrogen plasma. As-synthesized catalyst (denoted as *p*-Rh/Fe- Ni_3S_2 /NF) shows outstanding OER and HER activity; it reaches an OER/HER current density of 100 mA cm^{-2} at overpotentials of 237 mV and 108 mV , respectively. Its OER/HER activities do not fade significantly after more than 50 h of operation at a high current of 100 mA cm^{-2} , showing excellent durability. Detailed post-catalysis characterization and density functional theory (DFT) calculation reveal its unique Janus catalytic mechanism behind the Rh-enhanced OER and HER activity.

2. Experimental

2.1 Synthesis of *p*-Rh/Fe- Ni_3S_2 /NF and other catalysts

A piece of Ni foam (NF, $3 \text{ cm} \times 4 \text{ cm} \times 1.5 \text{ mm}$) was washed with deionized (DI) water, acetone, and 1 M of HCl for 30 min in sequence. It was then immersed in a mixed solution containing 20 mL of DMF, 8 mL of anhydrous ethanol, thioacetamide (TAA, 100 mg), $\text{Ni}(\text{NO}_3)_2 \cdot 6\text{H}_2\text{O}$ (0.768 mmol), and FeCl_3 (0.192 mmol) and transferred into a Teflon-lined stainless-steel autoclave. The autoclave was heated to $150 \text{ }^\circ\text{C}$ for 6 h in an electric oven. The NF was washed with DI water and dried at $60 \text{ }^\circ\text{C}$ to obtain Fe- Ni_3S_2 /NF.

As-synthesized Fe- Ni_3S_2 /NF was immersed in a solution containing 10 mL of DI water, $20 \text{ } \mu\text{L}$ of ethylene glycol, and $200 \text{ } \mu\text{L}$ of $\text{RhCl}_3 \cdot x\text{H}_2\text{O}$ (25 mg mL^{-1}) in a centrifuge tube. The tube was sealed and gently shaken for 48 h at room temperature. After washing and drying at $60 \text{ }^\circ\text{C}$ in a vacuum, the Rh/Fe- Ni_3S_2 /NF was prepared.

As-synthesized Rh/Fe- Ni_3S_2 /NF was placed in the reaction chamber with a pure H_2 atmosphere under a pressure of 18 Pa . At a H_2 flow rate of 30 mL min^{-1} , the hydrogen plasma was activated with an RF power at 45 W for 20 min treatment to obtain *p*-Rh/Fe- Ni_3S_2 /NF.

As-synthesized Rh/Fe- Ni_3S_2 /NF was placed in a tube furnace with H_2/Ar ($5:95$) at $350 \text{ }^\circ\text{C}$ for 2 h for annealing. After cooling to room temperature, Rh/Fe- Ni_3S_2 /NF-350 was prepared.

2.2 Preparation of RuO_2 /NF and Pt/C/NF

RuO_2 (2 mg , 99.9 wt\% from Alfa-Aesar) and Pt/C (2 mg , 20 wt\% from Alfa-Aesar) were respectively suspended in a mixture of absolute ethanol ($985 \text{ } \mu\text{L}$) and Nafion ($15 \text{ } \mu\text{L}$) to form a homogeneous catalyst ink under ultrasonication. Then the ink was dispersed onto NF ($1 \text{ cm} \times 1 \text{ cm}$) and dried at room temperature in a vacuum. The final RuO_2 and Pt loadings are $\sim 2 \text{ mg cm}^{-2}$ and 0.4 mg cm^{-2} , respectively.

2.3 Material characterization

The scanning electron microscopy (SEM) images of all samples were observed on a field emission SEM from JEOL (JSM-7800F). Transmission electron microscopy (TEM) observation was carried out on a JOEL TEM-2100 system after ultrasonically peeling off the materials from NF. The crystalline structures were probed by X-ray diffraction (XRD, Shimadzu XRD-7000 diffractometer with $\text{Cu K}\alpha$ line). X-ray photoelectron spectroscopy (XPS) measurement was performed on an ESCALAB 250Xi system from Thermo Fisher. Inductively coupled plasma atomic emission spectrometry (ICP-AES) measurements were performed on a PerkinElmer Optima 8000. Raman spectra were acquired using a LabRAM HR Evolution confocal Raman microscope from Horiba Jobin Yvon with a $50\times$ objective (LMPlanFL N $50\times/0.50$, Olympus). A laser of 532 nm with a power of 1 mW was used as the excitation light. Before measurements, the spectral shifts were calibrated using the 520.7 cm^{-1} peak of silicon. For electrochemical *in situ* Raman spectra, the catalyst was deposited on a graphitic rod as a working electrode. A graphitic rod counter electrode and a Hg/HgO reference electrode combined with a 760E potentiostat from CH Instruments, Shanghai, were employed for electrochemical measurements. Raman spectra were recorded from 300 to 1000 cm^{-1} at a resolution of 0.5 cm^{-1} .

2.4 Electrochemical measurements

All electrochemical experiments were tested using a 760E workstation (CH Instrument, USA) under a three-electrode setup. Freshly prepared 1.0 M KOH was used as the electrolyte solution. A graphite rod and a carefully calibrated Hg/HgO were used as the counter electrode and the reference electrode, respectively. All polarization curves were collected at a scan rate of 5 mV s^{-1} and presented after *iR* compensation unless otherwise specified. The electrochemical double-layer capacitance of a catalyst was estimated by the slope of a linear curve between non-faradaic capacitive current *vs.* scanning rate. The electrochemical surface area (ECSA) of a catalyst was calculated from the double-layer capacitance according to the equation, $\text{ECSA} = C_{\text{dl}}/C_s$, where C_s is the specific capacitance of a planar surface and is selected as 0.04 mF cm^{-2} in the present work.²³ Electrochemical impedance spectroscopy (EIS) measurements were carried out with an amplitude of 5 mV in the frequency range from 100 kHz to 0.01 Hz . Alkaline electrolyzer measurement was carried out in a standard two-electrode system without *iR* compensation.

2.5 DFT calculation

All DFT calculations were conducted using the Vienna *ab initio* simulation package (VASP). The generalized gradient approximation (GGA) functional of Perdew, Burke, and Ernzerhof (PBE) was employed for the electron exchange and correlation energy for structural relaxation.²⁴ The cut-off energy of plane-wave basis was set as 450 eV. The convergence criterion of total energy was converged to 1.0×10^{-4} eV per atom, and that of force on every atom was smaller than 0.02 eV \AA^{-1} . A vacuum width of 15 \AA along the Z axis was created to ensure negligible interaction.

3. Results and discussion

3.1. Characterization of *p*-Rh/Fe-Ni₃S₂/NF

As illustrated in Fig. 1a, *p*-Rh/Fe-Ni₃S₂/NF was synthesized *via* a three-step strategy. Fe-doped Ni₃S₂ nanosheets were first grown on NF (designated as Fe-Ni₃S₂/NF) *via* a hydrothermal reaction. After that, Rh atoms were impregnated on Fe-Ni₃S₂ nanosheets by immersing in RhCl₃ solution to obtain Rh/Fe-Ni₃S₂/NF. The driving force behind this incorporation is associated with the cation exchange and/or hetero-epitaxial growth of Rh₂S₃.²⁵ In the third step, Rh/Fe-Ni₃S₂/NF was processed in hydrogen plasma for 20 min to obtain *p*-Rh/Fe-Ni₃S₂/NF. The Rh loading is $\sim 44 \mu\text{g cm}^{-2}$ on the resultant *p*-Rh/Fe-Ni₃S₂/NF catalyst as measured by ICP-AES.

Fe-Ni₃S₂/NF shows dense and uniform nanosheets vertically grown on the NF skeleton and these ultrathin nanosheets interconnect with each other to form a porous layer (see the SEM image on the left in Fig. 1a). After Rh³⁺ impregnation, these nanosheets retained their morphology in Rh/Fe-Ni₃S₂/NF (SEM image in the middle in Fig. 1a). After hydrogen plasma

treatment, remarkably the space between the nanosheets becomes larger on resultant *p*-Rh/Fe-Ni₃S₂/NF (SEM image on the right in Fig. 1a); the lateral planes of nanosheets were destroyed, leaving behind the nanoframes with rough surfaces and increased thicknesses (see high-resolution SEM images in Fig. S1†). The morphological change is more obvious with prolonged treatment duration (Fig. S1†), suggesting the reconstruction of the nanosheets in hydrogen plasma due to the etching effect of highly corrosive H species produced *via* the ionization of H₂.^{26,27} This unique reticular structure of *p*-Rh/Fe-Ni₃S₂/NF is beneficial for mass transport and offers a large specific surface area for expediting the electrochemical reactions.^{28–30}

In the XRD pattern, all diffraction peaks of Fe-Ni₃S₂/NF nanosheets are well indexed to the rhombohedral phase Ni₃S₂ (PDF no. 44-1418) and metallic Ni (from NF substrate, PDF no. 04-0850, Fig. 1b). After incorporation of Rh, new diffraction peaks from the Rh₂S₃ phase (PDF no. 35-0736) appear besides those from Ni₃S₂ and metallic Ni.³¹ After hydrogen plasma treatment, the XRD pattern of *p*-Rh/Fe-Ni₃S₂/NF shows characteristic peaks of both Ni₃S₂ and Rh₂S₃ phases. Meanwhile, a new peak at 41° from metallic Rh (PDF no. 05-0685) appears, suggesting Rh formation under reductive hydrogen plasma. The weak characteristic peaks of the Rh₂S₃ phase suggest a low loading of Rh on the nanosheets and low Rh₂S₃ crystallinity.

In the Raman spectra in Fig. 1c, Fe-Ni₃S₂ shows several peaks in the 260–380 cm^{-1} range from the vibration of the Ni(Fe)-S bond. The broad peaks at around 530 cm^{-1} can be attributed to the Ni²⁺-O vibration formed on the surface of Fe-Ni₃S₂/NF in the air.³² After Rh incorporation, the Raman spectrum of Rh/Fe-Ni₃S₂/NF displays two additional peaks at 199 and 220 cm^{-1} , indicating the formation of a Rh-S bond, consistent with its XRD pattern in Fig. 1b.³³ After hydrogen plasma treatment, the peaks in the low wavenumber region were considerably weakened for *p*-Rh/Fe-Ni₃S₂/NF, indicating the partial damage of M-S (M = Rh, Ni and Fe) bonds due to the strong etching effect and reducing ability of hydrogen plasma; meanwhile a broad peak arises at around 500 cm^{-1} , implying the reduction of surface oxide species. During this process, partial surface S atoms were removed by active H radicals and abundant S vacancies were formed on the nanosheets, accompanied by the reduction of metal atoms and the decrease of sulfide crystallinity, in accordance with the XRD results in Fig. 1b.³⁴

The TEM image in Fig. 2a shows an individual *p*-Rh/Fe-Ni₃S₂ nanosheet with a lateral dimension of hundreds of nanometers. There are rich clusters embedded in the nanosheet. The diameter of most clusters is between 2.0 and 5.0 nm according to the statistical size distribution (inset in Fig. 2a). The high-resolution TEM images in Fig. 2b and c show several crystalline domains with clear lattice fringes for the clusters in the *p*-Rh/Fe-Ni₃S₂ nanosheet. Two crystalline domains assigned to metallic Rh and Rh₂S₃ are shown in Fig. 2b with clear Rh/Rh₂S₃ interfaces. In Fig. 2c, the clear lattice fringes could be assigned to Ni₃S₂ and Rh₂S₃, respectively. Meanwhile, some regions as indicated with white circles in Fig. 2b and c

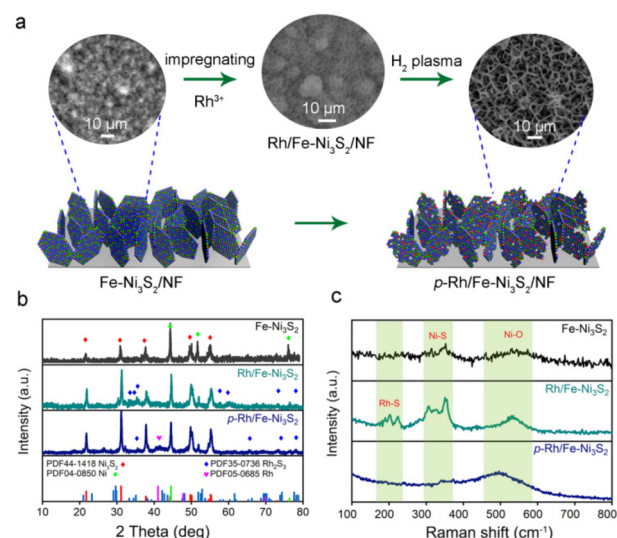


Fig. 1 (a) Schematic illustration of the three-step synthesis of *p*-Rh/Fe-Ni₃S₂/NF with SEM images of Fe-Ni₃S₂/NF (left), Rh/Fe-Ni₃S₂/NF (middle), and *p*-Rh/Fe-Ni₃S₂/NF (right); (b) XRD patterns and (c) Raman spectra of Fe-Ni₃S₂/NF, Rh/Fe-Ni₃S₂/NF, and *p*-Rh/Fe-Ni₃S₂/NF.

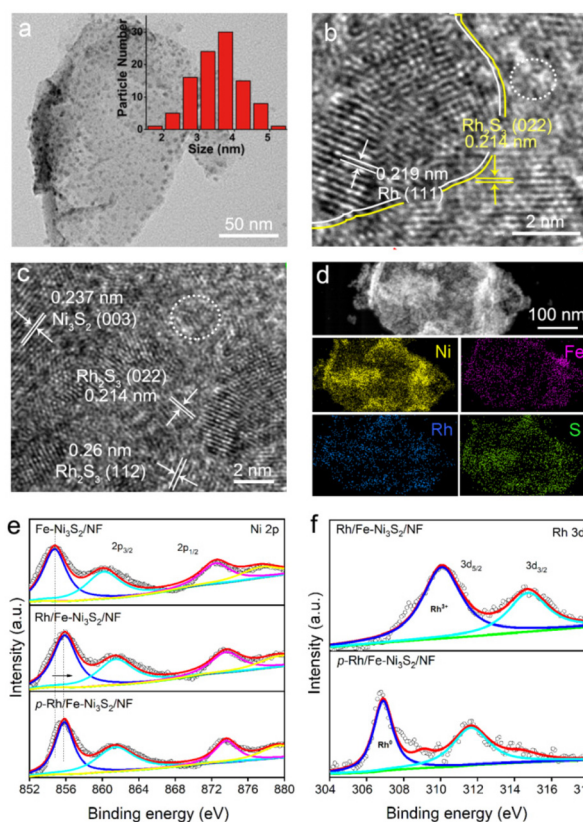


Fig. 2 TEM images (a, b, c) and elemental mapping images (d) of *p*-Rh/Fe-Ni₃S₂/NF; inset in (a) shows the size distribution of the nanoclusters; XPS Ni 2p (e) and Rh 3d spectra of *p*-Rh/Fe-Ni₃S₂/NF and other catalysts.

on the nanosheet show no clear lattice pattern, manifesting the amorphous nature of these areas as a result of hydrogen plasma treatment. The selected area electron diffraction (SAED) pattern in Fig. S2† shows three distinct diffraction rings from Ni₃S₂ (PDF44-1418), Rh₂S₃ (PDF35-0736), and metallic Rh (PDF05-0685), further verifying the hybrid compositions of the *p*-Rh/Fe-Ni₃S₂ nanosheets. Besides, the corresponding EDX mapping images (Fig. 2d) of an individual *p*-Rh/Fe-Ni₃S₂/NF nanosheet display that Ni, Fe, Rh, and S elements are distributed on the *p*-Rh/Fe-Ni₃S₂ nanosheets.

The Ni 2p XPS spectrum of Fe-Ni₃S₂/NF (Fig. 2e) shows two peaks at 872.3 and 854.8 eV, each with a satellite peak that can be assigned to Ni 2p_{1/2} and Ni 2p_{3/2}, respectively.^{13,35} After Rh incorporation, the binding energy of Ni 2p in Rh/Fe-Ni₃S₂/NF is considerably increased, indicative of the electronic interaction between Ni and Rh. In the Rh 3d spectrum of Rh/Fe-Ni₃S₂/NF (Fig. 2f), two peaks at 309.9 and 314.5 eV are well assigned to Rh 3d_{5/2} and 3d_{3/2}. Both peaks of Rh 3d in *p*-Rh/Fe-Ni₃S₂/NF are negatively shifted after hydrogen plasma treatment, suggesting the reduction of Rh³⁺ to Rh (0).^{13,36,37} The binding energy of Ni 2p remains unchanged after plasma treatment, which may be due to the fact that Rh is easier to be reduced than Ni and plasma reduced metallic Ni, if any, is apt to be re-oxidized after exposure to air. For S 2p, the peak intensity at 168.2 eV from the oxidized S species on *p*-Rh/Fe-Ni₃S₂/NF

NF is considerably decreased compared to Fe-Ni₃S₂/NF and Rh/Fe-Ni₃S₂/NF (Fig. S3†), indicating the reduction of SO_x species by hydrogen plasma, in line with the Raman spectra in Fig. 1c. For Fe 2p spectra, no evident difference is observed among *p*-Rh/Fe-Ni₃S₂/NF, Fe-Ni₃S₂/NF, and Rh/Fe-Ni₃S₂/NF (Fig. S4†).

3.2. OER performance of *p*-Rh/Fe-Ni₃S₂/NF

The OER performance of *p*-Rh/Fe-Ni₃S₂/NF was evaluated in 1.0 M KOH. As shown in Fig. 3a, all the catalysts show an anodic peak at ~1.32 V on linear scan voltammetry (LSV) curves due to the nominal oxidation of Ni²⁺ to Ni³⁺, followed by a sharply increased anodic OER current with a further polarized potential. *p*-Rh/Fe-Ni₃S₂/NF clearly shows advantageous OER activity over Fe-Ni₃S₂/NF, Rh/Fe-Ni₃S₂/NF, and RuO₂/NF. To achieve 100, 200, and 300 mA cm⁻² current, *p*-Rh/Fe-Ni₃S₂/NF needs overpotentials of 237, 251, and 259 mV, much lower than those of Fe-Ni₃S₂/NF, Rh/Fe-Ni₃S₂/NF, and RuO₂/NF, respectively (Fig. 3b). The Tafel slopes of all catalysts were calculated and are presented in Fig. 3c, showing the lowest Tafel slope of 49 mV dec⁻¹ of *p*-Rh/Fe-Ni₃S₂/NF, indicating its favorable OER kinetics over its rivals. In EIS collected at 1.524 V shown in Fig. 3d, *p*-Rh/Fe-Ni₃S₂/NF possesses a smaller charge transfer resistance (R_{ct}) than its two analogues,

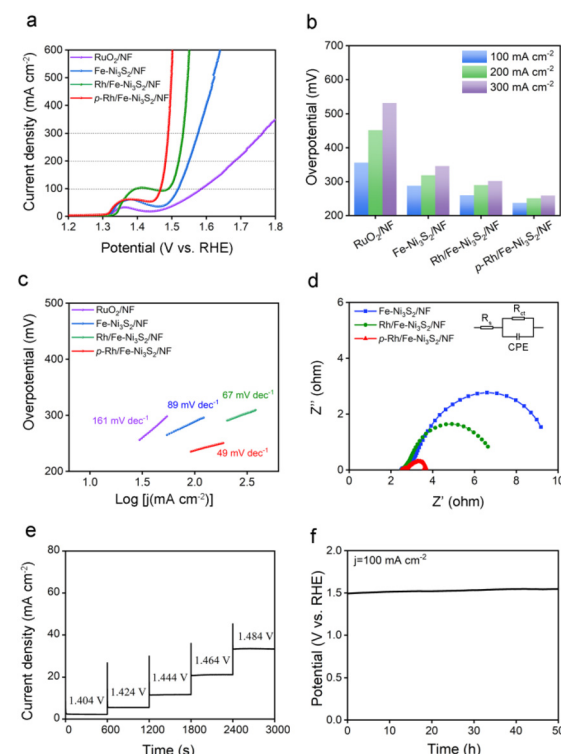


Fig. 3 OER performance of *p*-Rh/Fe-Ni₃S₂/NF in 1 M KOH. (a) *iR*-compensated polarization curves at 5 mV s⁻¹, (b) overpotentials required at a given current density, (c) Tafel plots, (d) Nyquist plots of various catalysts collected at 1.524 V with the corresponding equivalent circuit, (e) multi-step chronoamperometric curve (without *iR* correction), and (f) chronoamperometric curve of *p*-Rh/Fe-Ni₃S₂/NF at 100 mA cm⁻².

indicating faster OER kinetics. This comparison clearly demonstrates that Rh-incorporation in Fe-Ni₃S₂/NF efficiently enhances the OER performance of the resultant Rh/Fe-Ni₃S₂/NF, and subsequent hydrogen plasma treatment further promotes the catalytic activity.

To differentiate the current from the OER and oxidation of Ni²⁺, a multi-step chronoamperometric measurement was carried out. As shown in Fig. 3e, when the potential of the *p*-Rh/Fe-Ni₃S₂/NF electrode was held at 1.404 V, nearly constant anodic current was observed on the electrode for 600 s. Stepping to 1.424 V and higher results in a prompt increase in the anodic current, verifying that the observed anodic current is indeed from the OER but not from possible oxidation of surface metal species as the latter cannot afford such high and continuous currents. Chronopotentiometric measurement in Fig. 3f further highlights the excellent durability of *p*-Rh/Fe-Ni₃S₂/NF. The potential increases slightly from 1.49 V to 1.54 V during 50 h of uninterrupted electrolysis at a constant current density of 100 mA cm⁻².

3.3. Mechanism of enhanced OER activity of *p*-Rh/Fe-Ni₃S₂/NF

To investigate the intrinsic OER activity of *p*-Rh/Fe-Ni₃S₂/NF, the electrochemical surface areas (ECSAs) of these catalysts were measured by the double-layer capacitance (C_{dl}) method. As shown in Fig. S5,† *p*-Rh/Fe-Ni₃S₂/NF exhibits the highest C_{dl} (25.53 mF cm⁻²) compared to those of Rh/Fe-Ni₃S₂/NF and Fe-Ni₃S₂/NF, suggesting an increase in the active area of *p*-Rh/Fe-Ni₃S₂/NF to promote its OER performance.³⁸ Remarkably, the intrinsic OER activity of *p*-Rh/Fe-Ni₃S₂/NF is still higher than its two rivals after ECSA-normalization (Fig. S6†), manifesting that its high OER performance is associated not only with its high surface areas but also with its promoted intrinsic activity.

Post-OER characterization was carried out to investigate the possible mechanism of the enhanced intrinsic activity of *p*-Rh/Fe-Ni₃S₂/NF. From the SEM image in Fig. S7,† the *p*-Rh/Fe-Ni₃S₂/NF nanosheets become clumpy nanoparticles after the long-term OER, indicating dramatic reconstruction of the nanostructure during the harsh OER process. The Rh content in the catalyst remains almost unchanged (\sim 42 μ g cm⁻²) after the long-term OER, as measured by ICP-AES, indicating negligible Rh dissolution. The XRD pattern in Fig. 4a proves that after the long-term OER, *p*-Rh/Fe-Ni₃S₂/NF exhibits newly-appeared peaks of NiOOH and Rh₂O₃ (PDF no. 41-0541). The characteristic peaks of Ni₃S₂ remain but those from metallic Rh and Rh₂S₃ disappear. The Rh 3d XPS spectrum of *p*-Rh/Fe-Ni₃S₂/NF after the OER demonstrates positively shifted binding energy (Fig. S8†), again suggesting the formation of the Rh₂O₃ phase from metallic Rh and Rh₂S₃ after the OER process. The TEM image in Fig. S9† also shows that the pristine nanosheet morphology was partly destroyed, and some nanoparticles were retained on the nanosheets to form agglomerations, in good agreement with SEM in Fig. S7.† The high-resolution TEM image in Fig. 4b displays clear lattice fringes with inter-planar distances corresponding to the NiOOH (101), Rh₂O₃ (202) and Ni₃S₂ (110) planes, respectively.

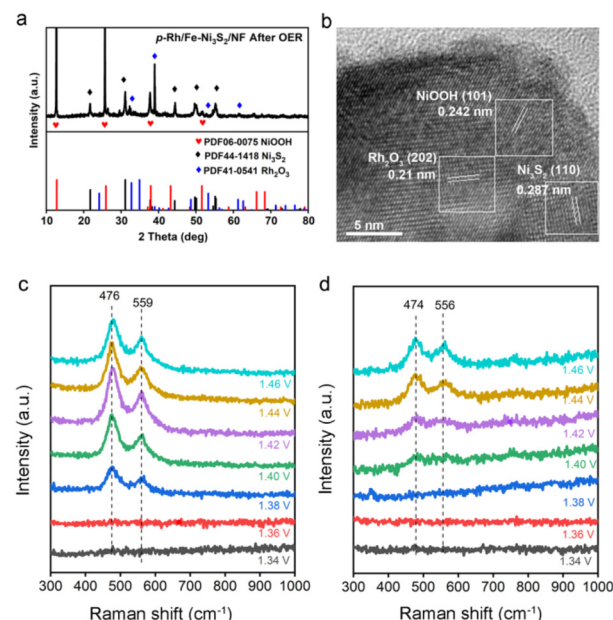


Fig. 4 Post-OER characterization of *p*-Rh/Fe-Ni₃S₂/NF after 50 h of the OER at 100 mA cm⁻²: (a) XRD pattern and (b) TEM images. (c and d) OER *in situ* Raman spectra of (c) *p*-Rh/Fe-Ni₃S₂/NF and (d) Fe-Ni₃S₂/NF at different polarized potentials.

The SAED pattern confirms the same crystalline compositions of *p*-Rh/Fe-Ni₃S₂/NF after the OER (Fig. S10†). These post-OER characterization studies unambiguously suggest that *p*-Rh/Fe-Ni₃S₂/NF experiences surface transformation and nanostructure reconstruction during the long-term OER; NiOOH and Rh₂O₃ are *in situ* formed on *p*-Rh/Fe-Ni₃S₂/NF during the OER;^{8,10} meanwhile, the partial Ni₃S₂ phase survives to support the catalytically active phase in the OER.

In situ Raman spectroscopy was used to investigate the surface reconstruction of *p*-Rh/Fe-Ni₃S₂/NF under OER *operando* conditions. As shown in Fig. 4c, there are two obvious peaks at 476 and 559 cm⁻¹ on *p*-Rh/Fe-Ni₃S₂/NF at 1.38 V and higher, corresponding to two vibration modes (e_g bending and A_{1g} stretching) of the Ni³⁺-O bond, both of which indicate the formation of the NiOOH phase at the anodic potential.^{2,8,39} The Fe-Ni₃S₂/NF catalyst also exhibits similar potential-dependent Raman spectra, as in Fig. 4d. Notably, the e_g and A_{1g} wavenumbers of *p*-Rh/Fe-Ni₃S₂/NF are shifted to higher values compared to Fe-Ni₃S₂/NF, which implies that the Ni³⁺-O bond in *p*-Rh/Fe-Ni₃S₂/NF was compressed to possess a shorter bond length.⁴⁰ The NiOOH formation starts at 1.38 V for *p*-Rh/Fe-Ni₃S₂/NF, which is earlier than that of Fe-Ni₃S₂/NF (1.42 V), manifesting that the Rh incorporation is beneficial for Ni oxidation, which is able to promote the OER process.⁴¹ The intensity ratio between the A_{1g} peak (\sim 560 cm⁻¹) and the e_g peak (\sim 475 cm⁻¹) of *p*-Rh/Fe-Ni₃S₂/NF at 1.46 V reaches 0.64, which is considerably lower than that of Fe-Ni₃S₂/NF (0.77) at the same potential, indicating the higher order level of NiOOH.^{8,40} Previous work has revealed that too many Fe dopants in NiOOH result in a higher disorder level and impair the OER activity.^{8,40} In the present work, it is believed that Rh atoms

are doped into the NiOOH matrix to form di- μ -oxo bridged Ni-O-Rh sites while keeping the NiOOH with a high order level to enhance the OER activity. The Rh atom possesses higher electron affinity compared to Fe and Ni atoms, resulting in a shorter and stronger Ni-O bond in Ni-O-Rh and a lower oxidative potential for the conversion of Ni^{2+} to Ni^{3+} . The formed Ni-O-Rh sites together with the Ni-O-Fe sites contribute to the OER activity of *p*-Rh/Fe-Ni₃S₂/NF. Without hydrogen plasma, such active sites cannot be formed efficiently, and that is the case for Rh/Fe-Ni₃S₂/NF.

DFT calculations were performed to rationalize the enhanced OER activity of *p*-Rh/Fe-Ni₃S₂/NF. Rh/Fe-doped NiOOH was employed to model the OER process in contrast to Fe-doped NiOOH. The optimal surfaces on two catalysts were first calculated and determined, respectively, as shown in Fig. 5a and b. A conventional four-step mechanism (*OH, *O, and *OOH; * denotes the active site) was adopted to describe the OER process.^{42,43} For Fe-doped NiOOH without Rh, the process of *OH to *O is the rate determining step of the OER (Fig. 5c), and the overpotential is calculated to be 0.71 eV, which is lower than that of the pure NiOOH surface (Fig. S11†), suggesting a tremendous improvement of Fe-doping on the OER activity. With Rh incorporated, the rate determining step remains unchanged but the overpotential required further decreases to 0.63 eV (Fig. 5d), indicating that Rh-doping strengthens the binding of *O to facilitate the rate determining step and accelerates the whole OER process.

3.4. HER performance of *p*-Rh/Fe-Ni₃S₂/NF

p-Rh/Fe-Ni₃S₂/NF shows excellent HER activity in alkaline solution as well. As depicted in Fig. 6a, Fe-Ni₃S₂/NF requires an

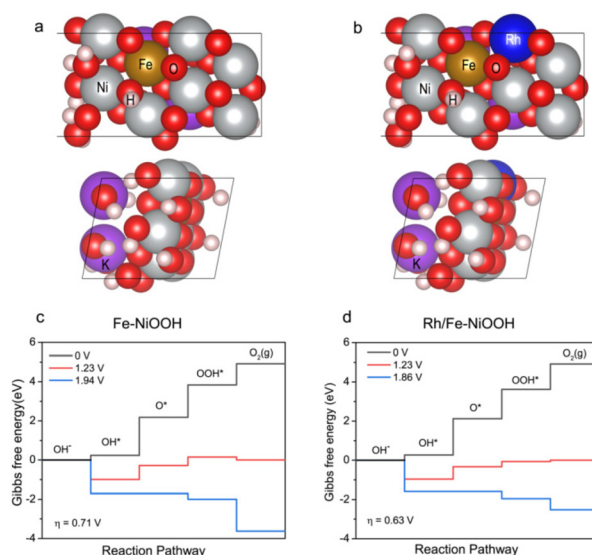


Fig. 5 DFT calculation of the OER process on Fe-doped NiOOH and Rh/Fe-doped NiOOH surfaces. Side (upper) and top views (bottom) of the model surfaces of Fe-doped NiOOH (a) and Rh/Fe-doped NiOOH (b); free energy diagrams of the OER on Fe-doped NiOOH (c) and Rh/Fe-doped NiOOH (d).

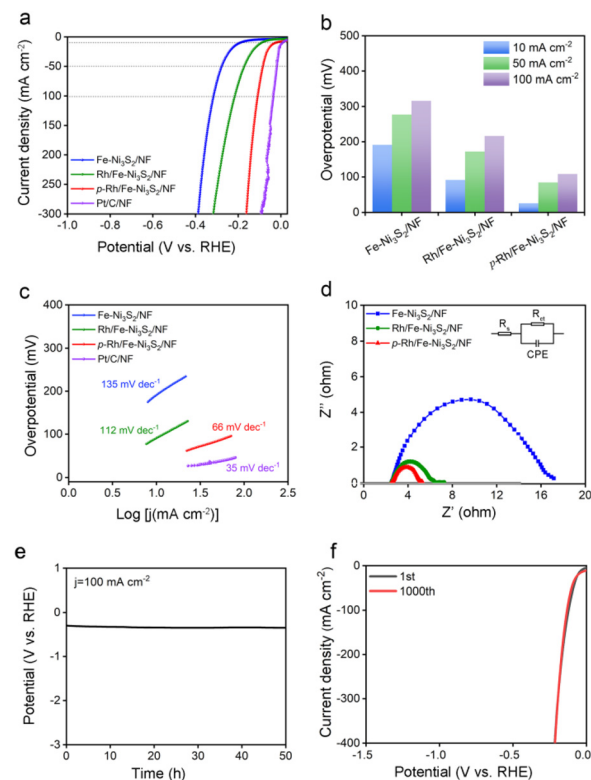


Fig. 6 HER performance of *p*-Rh/Fe-Ni₃S₂/NF in comparison to other catalysts in 1 M KOH. (a) *iR*-corrected polarization curves at 5 mV s^{-1} , (b) overpotentials required at a given current density, (c) Tafel plots, (d) Nyquist plots of various catalysts collected at -0.296 V with an equivalent circuit, (e) chronopotentiometry curve at 100 mA cm^{-2} , and (f) LSV curves of *p*-Rh/Fe-Ni₃S₂/NF before and after 1000 cycles of CV, scanning rate: 5 mV s^{-1} .

overpotential of 191 mV to achieve an HER current of 10 mA cm^{-2} , indicating its limited HER activity. After Rh incorporation, the overpotential of Rh/Fe-Ni₃S₂/NF largely decreases to 91 mV at the same current density. *p*-Rh/Fe-Ni₃S₂/NF itself, in sharp contrast, needs overpotentials of only 25 and 108 mV to achieve HER current values of 10 and 100 mA cm^{-2} , respectively (Fig. 6b). Although still inferior to the benchmark Pt/C catalyst, it significantly outperforms those of Fe-Ni₃S₂/NF and Rh/Fe-Ni₃S₂/NF, indicating the important role of Rh incorporation and hydrogen plasma treatment. The Tafel slope of the *p*-Rh/Fe-Ni₃S₂/NF was found to be 66 mV dec^{-1} , which is smaller than that of Rh/Fe-Ni₃S₂/NF and Fe-Ni₃S₂/NF, as shown in Fig. 6c, indicating the fast HER kinetics of *p*-Rh/Fe-Ni₃S₂/NF. The EIS spectrum of *p*-Rh/Fe-Ni₃S₂/NF in Fig. 6d shows a smaller charge transfer resistance than those of Rh/Fe-Ni₃S₂/NF and Fe-Ni₃S₂/NF due to the promotion effect of Rh-doping and plasma treatment on HER activity. Meanwhile, during 50 h of HER operation at a constant current of 100 mA cm^{-2} , the overpotential of *p*-Rh/Fe-Ni₃S₂/NF slightly increases by 49 mV (Fig. 6e). The polarization curve of *p*-Rh/Fe-Ni₃S₂/NF after a 1000-cycle accelerated stability test completely overlaps with that of the pristine one (Fig. 6f), again implying its excellent HER durability.

3.5. Mechanism of enhanced HER activity of *p*-Rh/Fe-Ni₃S₂/NF

As shown in Fig. S12,† *p*-Rh/Fe-Ni₃S₂/NF displays a higher ECSA than Rh/Fe-Ni₃S₂/NF and Fe-Ni₃S₂/NF upon an HER test, suggesting that Rh incorporation and subsequent hydrogen plasma treatment introduce abundant defects and vacancies in the nanosheets.⁴⁴ ECSA-normalized LSV curves in Fig. S13† further confirm that the intrinsic HER activity of *p*-Rh/Fe-Ni₃S₂/NF is also improved compared to Rh/Fe-Ni₃S₂/NF and Fe-Ni₃S₂/NF. The XRD pattern (Fig. S14†) shows that all the diffraction peaks of *p*-Rh/Fe-Ni₃S₂/NF remain after HER catalysis; no new crystalline phase was detected. At the same time, it maintains a nanosheet morphology after the long-term HER according to the SEM image in Fig. S15.† In XPS spectra (Fig. S16†), no obvious shift in the binding energy of Ni 2p, Rh 3d, Fe 2p and S 2p was observed for *p*-Rh/Fe-Ni₃S₂/NF after long-term HER catalysis. The Rh content in the catalyst slightly decreases to ~34 µg cm⁻² after 50 h of the HER, indicating mild Rh leakage. Therefore, *p*-Rh/Fe-Ni₃S₂/NF preserves its compositional and structural properties during the HER, which is in sharp contrast with the situation for the OER.

Rh₂S₃ has been reported to be highly active for the HER and hydrogen oxidation reaction (HOR).^{25,33} Meanwhile, metallic Rh supported on various substrates such as Si, SWCNTs, MoS₂, etc. in the form of clusters, nanoparticles or single atoms demonstrates excellent HER activity.^{37,45,46} In the present work the enhanced HER activity of *p*-Rh/Fe-Ni₃S₂/NF over Rh/Fe-Ni₃S₂/NF and Fe-Ni₃S₂/NF suggests that the co-existence of metallic Rh and Rh₂S₃ is critical for the HER activity. Therefore, the Rh/Rh₂S₃ heterostructure may be responsible for the HER activity due to its optimal hydrogen adsorption strength.

DFT calculation was carried out to verify this synergistic effect between Rh and Rh₂S₃. The optimal structural model of the Rh₂S₃/Rh interface was first determined by considering the lattice matching of Rh and Rh₂S₃ planes, as shown in Fig. 7a

(model surfaces of pure Rh and pure Rh₂S₃ shown in Fig. S17†). At such a heterointerface, the water adsorption energy was first calculated as it is important to initiate the HER in an alkaline environment.⁴⁷ As in Fig. 7b, the H₂O adsorption energies on the Rh part, Rh₂S₃ part and interface of the Rh₂S₃/Rh heterojunction are -0.570, -0.592, and -0.659 eV, respectively; all are higher than those of pure Rh₂S₃ (-0.544 eV) and Rh (-0.447 eV), suggesting stronger H₂O adsorption energy, which is capable of speeding up the HER process.⁴⁸ The hydrogen adsorption energy (ΔG_{H^*}) on the model surface was further calculated (Fig. 7c). The ΔG_{H^*} on the interface of the Rh₂S₃/Rh heterojunction is ~-0.05 eV, which is smaller than that on the Rh surface (-0.185 eV) and the Rh₂S₃ part (0.476 eV) of the Rh₂S₃/Rh heterojunction, and is also lower than that on pure Rh₂S₃ (0.540 eV) and Rh (-0.272 eV). This result indicates that the most active site is the Rh-Rh₂S₃ interface, where the favorable H^{*} adsorption energy leads to excellent HER activity. Notably, the charge density differential image reveals that a strong interaction occurred at the interface of Rh₂S₃/Rh (Fig. S18†), leading to lattice distortion and electron rearrangement of Rh₂S₃ and Rh, and improving their HER activity compared to their corresponding pure phases.

3.6. Influence of H₂ plasma treatment

To further clarify the effect of H₂ plasma treatment on the synthesis of *p*-Rh/Fe-Ni₃S₂/NF, thermal treatment of Rh/Fe-Ni₃S₂ was carried out in a H₂/Ar atmosphere at 350 °C to obtain the catalyst of Rh/Fe-Ni₃S₂-350. The XRD pattern indicates the same crystal phases (metallic Rh, Rh₂S₃, and Ni₃S₂) of as-produced Rh/Fe-Ni₃S₂-350 as *p*-Rh/Fe-Ni₃S₂/NF, suggesting the partial reduction of Rh₂S₃ to metallic Rh after thermal treatment (Fig. S19†). However, the Rh/Fe-Ni₃S₂-350 is inferior to the *p*-Rh/Fe-Ni₃S₂/NF in terms of HER and OER activity (Fig. S20†), even though both catalysts are composed of the same components. This comparison implies that plasma treatment for the synthesis of *p*-Rh/Fe-Ni₃S₂/NF is necessary and cannot be displaced by thermal annealing in H₂. Meanwhile, the duration of H₂ plasma treatment was also investigated and an optimal duration of 20 min was found, at which the resultant *p*-Rh/Fe-Ni₃S₂/NF exhibits the best HER and OER performance (Fig. S21†). Ar plasma was also investigated but it cannot afford the same enhancement effect on OER or HER activity as hydrogen plasma (Fig. S22†). These observations indicate that H₂ plasma treatment is used not only to simply reduce some sulfides to metal, but also results in rich surface defects and nanostructure reconstruction to facilitate electrocatalysis; there is a balance between the etching/reducing effects of plasma treatment to maximize the electrocatalytic activity of this catalyst.

3.7. Overall water splitting of *p*-Rh/Fe-Ni₃S₂/NF

Electrochemical evaluations suggest that *p*-Rh/Fe-Ni₃S₂/NF is a highly active HER/OER bifunctional electrocatalyst even though its real active phase is different under two electrochemical environments. As shown in Fig. 8a, *p*-Rh/Fe-Ni₃S₂/NF

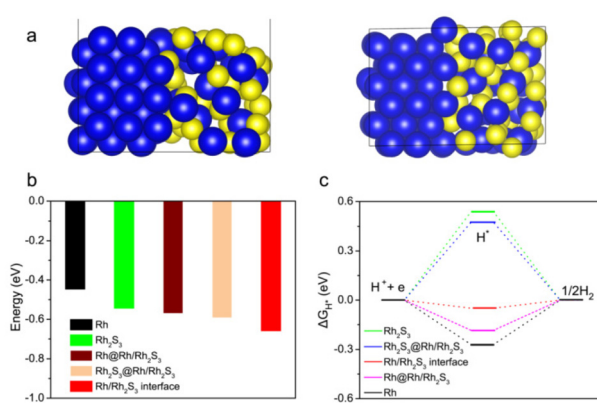


Fig. 7 DFT calculation of the HER process on *p*-Rh/Fe-Ni₃S₂/NF. (a) Side (left) and top view (right) of the model surface used for the Rh₂S₃/Rh heterointerface. Blue and yellow balls represent Rh and S atoms, respectively; calculated water adsorption energies (b) and ΔG_{H^*} (c) on Rh₂S₃/Rh, Rh₂S₃ and Rh.

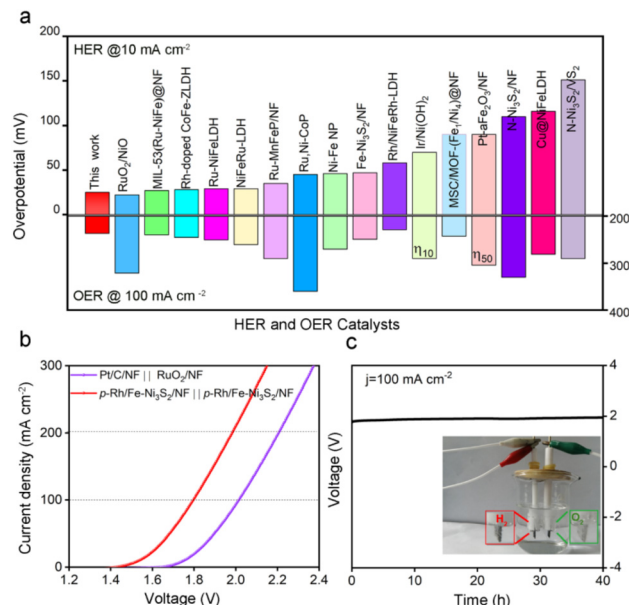


Fig. 8 Performance comparison of *p*-Rh/Fe-Ni₃S₂/NF and other bifunctional catalysts. (a) Overpotential at a current density of 10 mA cm⁻² for the HER and 100 mA cm⁻² for the OER, respectively. (b) polarization curves (without *iR*-compensation) of the *p*-Rh/Fe-Ni₃S₂/NF||*p*-Rh/Fe-Ni₃S₂/NF and Pt/C/NF||RuO₂/NF alkaline water electrolyzer at 5 mV s⁻¹; (c) chronopotentiometric curve of *p*-Rh/Fe-Ni₃S₂/NF||*p*-Rh/Fe-Ni₃S₂/NF at 100 mA cm⁻² without *iR*-compensation. The inset in (c) shows the optical image of this electrolyzer under operation.

was among the best HER/OER bifunctional catalysts reported in the literature.^{10,16,22,49–62}

Due to its good OER/HER activity, *p*-Rh/Fe-Ni₃S₂/NF was employed to assemble an alkaline electrolyzer as both an anodic and a cathodic catalyst. As shown in Fig. 8b, the assembled electrolyzer achieves higher electrolytic current than the one with commercial Pt/C and RuO₂ on NF as cathodic and anodic catalysts at the same cell voltage. It needs a low cell voltage of 1.79 V to obtain an electrolytic current of 100 mA cm⁻², while the precious-metal based one needs 2.0 V to achieve the same current, unambiguously confirming the high activity of *p*-Rh/Fe-Ni₃S₂/NF. Meanwhile, this electrolyzer is able to stably operate at 100 mA cm⁻² for 40 h (Fig. 8c), showing excellent catalytic stability of *p*-Rh/Fe-Ni₃S₂/NF as the bifunctional catalyst. The faradaic efficiency of *p*-Rh/Fe-Ni₃S₂/NF was found to be close to 100% by a drainage method, as shown in Fig. S23.[†]

4. Conclusions

In summary, we reported *p*-Rh/Fe-Ni₃S₂/NF synthesized *via* wet impregnation and subsequent hydrogen plasma treatment as an excellent HER/OER bifunctional catalyst. By introducing a low content of Rh, the resultant *p*-Rh/Fe-Ni₃S₂/NF exhibits outstanding HER and OER catalytic performance in alkaline media. Remarkably, a unique Janus catalytic mechanism is

revealed for *p*-Rh/Fe-Ni₃S₂/NF; it catalyzes the OER and HER with different active phases. For the OER, the doped Rh atoms in the *in situ* formed Ni oxyhydroxide matrix collaborate with the Ni-O-Fe sites to enhance the OER activity; for the HER, the heterostructured Rh/Rh₂S₃ clusters offer active centers while the Ni₃S₂ nanosheets offer high conductivity and large surface areas. Hydrogen plasma was demonstrated to manipulate the compositional and structural properties of a catalyst under mild conditions with broad flexibility and good controllability, thus providing a novel and elegant tool for fabricating efficient catalysts.

Conflicts of interest

There are no conflicts to declare.

Acknowledgements

The financial support from the National Natural Science Foundation of China (No. 22074125), the Natural Science Foundation Project of CQ CSTC (cstc2021jcyj-msxmX1165) and The Innovation Platform for Academicians of Hainan Province is gratefully acknowledged.

References

- 1 Z. W. Seh, J. Kibsgaard, C. F. Dickens, I. B. Chorkendorff, J. K. Norskov and T. F. Jaramillo, Combining theory and experiment in electrocatalysis: Insights into materials design, *Science*, 2017, **355**, eaad4998.
- 2 G. Liu, M. Wang, Y. Xu, X. Wang, X. Li, J. Liu, X. Cui and L. Jiang, Porous CoP/Co₂P heterostructure for efficient hydrogen evolution and application in magnesium/seawater battery, *J. Power Sources*, 2021, **486**, 229351.
- 3 Z. Li, X. Dou, Y. Zhao and C. Wu, Enhanced oxygen evolution reaction of metallic nickel phosphide nanosheets by surface modification, *Inorg. Chem. Front.*, 2016, **3**, 1021–1027.
- 4 R. Gao and D. Yan, Recent Development of Ni/Fe-Based Micro/Nanostructures toward Photo/Electrochemical Water Oxidation, *Adv. Energy Mater.*, 2020, **10**, 1900954.
- 5 M. Rinawati, Y.-X. Wang, K.-Y. Chen and M.-H. Yeh, Designing a spontaneously deriving NiFe-LDH from bimetallic MOF-74 as an electrocatalyst for oxygen evolution reaction in alkaline solution, *Chem. Eng. J.*, 2021, **423**, 130204.
- 6 B. S. Yeo and A. T. Bell, In Situ Raman Study of Nickel Oxide and Gold-Supported Nickel Oxide Catalysts for the Electrochemical Evolution of Oxygen, *J. Phys. Chem. C*, 2012, **116**, 8394–8400.
- 7 J. Du, A. Yu, Z. Zou and C. Xu, One-pot synthesis of iron-nickel-selenide nanorods for efficient and durable electrochemical oxygen evolution, *Inorg. Chem. Front.*, 2018, **5**, 814–818.

8 L. Yi, Y. Niu, B. Feng, M. Zhao and W. Hu, Simultaneous phase transformation and doping via a unique photochemical-electrochemical strategy to achieve a highly active Fe-doped Ni oxyhydroxide oxygen evolution catalyst, *J. Mater. Chem. A*, 2021, **9**, 4213–4220.

9 D. Y. Chung, P. P. Lopes, P. F. B. D. Martins, H. He, T. Kawaguchi, P. Zapol, H. You, D. Tripkovic, D. Strmcnik, Y. Zhu, S. Seifert, S. Lee, V. R. Stamenkovic and N. M. Markovic, Dynamic stability of active sites in hydr(oxy)oxides for the oxygen evolution reaction, *Nat. Energy*, 2020, **5**, 222–230.

10 B. Zhang, C. Zhu, Z. Wu, E. Stavitski, Y. H. Lui, T.-H. Kim, H. Liu, L. Huang, X. Luan, L. Zhou, K. Jiang, W. Huang, S. Hu, H. Wang and J. S. Francisco, Integrating Rh Species with NiFe-Layered Double Hydroxide for Overall Water Splitting, *Nano Lett.*, 2020, **20**, 136–144.

11 W. Jin, H. Wu, W. Cai, B. Jia, M. Batmunkh, Z. Wu and T. Ma, Evolution of interfacial coupling interaction of Ni-Ru species for pH-universal water splitting, *Chem. Eng. J.*, 2021, **426**, 130762.

12 Z. Li, K. Wang, X. Tan, X. Liu, G. Wang, G. Xie and L. Jiang, Defect-enriched multistage skeleton morphology Ni-Fe-P-Ni₃S₂ heterogeneous catalyst on Ni foam for efficient overall water splitting, *Chem. Eng. J.*, 2021, **424**, 130390.

13 H. Sun, W. Zhang, J.-G. Li, Z. Li, X. Ao, K.-H. Xue, K. K. Ostrikov, J. Tang and C. Wang, Rh-engineered ultra-thin NiFe-LDH nanosheets enable highly-efficient overall water splitting and urea electrolysis, *Appl. Catal., B*, 2021, **284**, 119740.

14 K. Wang, B. Li, J. Ren, W. Chen, J. Cui, W. Wei and P. Qu, Ru@Ni₃S₂ nanorod arrays as highly efficient electrocatalysts for the alkaline hydrogen evolution reaction, *Inorg. Chem. Front.*, 2022, **9**, 3885.

15 Q. Wang, X. Huang, Z. L. Zhao, M. Wang, B. Xiang, J. Li, Z. Feng, H. Xu and M. Gu, Ultrahigh-Loading of Ir Single Atoms on NiO Matrix to Dramatically Enhance Oxygen Evolution Reaction, *J. Am. Chem. Soc.*, 2020, **142**, 7425–7433.

16 G. Zhao, P. Li, N. Cheng, S. X. Dou and W. Sun, An Ir/Ni(OH)₂ Heterostructured Electrocatalyst for the Oxygen Evolution Reaction: Breaking the Scaling Relation, Stabilizing Iridium(v), and Beyond, *Adv. Mater.*, 2020, **32**, 2000872.

17 P. Su, W. Pei, X. Wang, Y. Ma, Q. Jiang, J. Liang, S. Zhou, J. Zhao, J. Liu and G. Q. Lu, Exceptional Electrochemical HER Performance with Enhanced Electron Transfer between Ru Nanoparticles and Single Atoms Dispersed on a Carbon Substrate, *Angew. Chem., Int. Ed.*, 2021, **60**, 16044.

18 Y. Sun, Z. Xue, Q. Liu, Y. Jia, Y. Li, K. Liu, Y. Lin, M. Liu, G. Li and C.-Y. Su, Modulating electronic structure of metal-organic frameworks by introducing atomically dispersed Ru for efficient hydrogen evolution, *Nat. Commun.*, 2021, **12**, 1369.

19 L.-L. Feng, G. Yu, Y. Wu, G.-D. Li, H. Li, Y. Sun, T. Asefa, W. Chen and X. Zou, High-Index Faceted Ni₃S₂ Nanosheet Arrays as Highly Active and Ultrastable Electrocatalysts for Water Splitting, *J. Am. Chem. Soc.*, 2015, **137**, 14023.

20 X. Zou, Y. Liu, G.-D. Li, Y. Wu, D.-P. Liu, W. Li, H.-W. Li, D. Wang, Y. Zhang and X. Zou, Ultrafast Formation of Amorphous Bimetallic Hydroxide Films on 3D Conductive Sulfide Nanoarrays for Large-Current-Density Oxygen Evolution Electrocatalysis, *Adv. Mater.*, 2017, **29**, 1700404.

21 Y. Wu, Y. Li, M. Yuan, H. Hao, X. San, Z. Lv, L. Xu and B. Wei, Operando capturing of surface self-reconstruction of Ni₃S₂/FeNi₂S₄ hybrid nanosheet array for overall water splitting, *Chem. Eng. J.*, 2022, **427**, 131944.

22 J. Liu, Y. Zheng, Y. Jiao, Z. Wang, Z. Lu, A. Vasileff and S.-Z. Qiao, NiO as a Bifunctional Promoter for RuO₂ toward Superior Overall Water Splitting, *Small*, 2018, **14**, 1704073.

23 C. C. L. McCrory, S. Jung, J. C. Peters and T. F. Jaramillo, Benchmarking Heterogeneous Electrocatalysts for the Oxygen Evolution Reaction, *J. Am. Chem. Soc.*, 2013, **135**, 16977.

24 G. Zhou, M. Li, Y. Li, H. Dong, D. Sun, X. Liu, L. Xu, Z. Tian and Y. Tang, Regulating the Electronic Structure of CoP Nanosheets by O Incorporation for High-Efficiency Electrochemical Overall Water Splitting, *Adv. Funct. Mater.*, 2020, **30**, 1905252.

25 D. Yoon, B. Seo, J. Lee, K. S. Nam, B. Kim, S. Park, H. Baik, S. H. Joo and K. Lee, Facet-controlled hollow Rh₂S₃ hexagonal nanoprisms as highly active and structurally robust catalysts toward hydrogen evolution reaction, *Energy Environ. Sci.*, 2016, **9**, 850.

26 Y. Xu, H. Lv, H. Lu, Q. Quan, W. Li, X. Cui, G. Liu and L. Jiang, Mg/seawater batteries driven self-powered direct seawater electrolysis systems for hydrogen production, *Nano Energy*, 2022, **98**, 107295.

27 W. Li, D. Wang, Y. Zhang, L. Tao, T. Wang, Y. Zou, Y. Wang, R. Chen and S. Wang, Defect Engineering for Fuel-Cell Electrocatalysts, *Adv. Mater.*, 2020, **32**, 1907879.

28 L. Zeng, K. Sun, X. Wang, Y. Liu, Y. Pan, Z. Liu, D. Cao, Y. Song, S. Liu and C. Liu, Three-dimensional-networked Ni₂P/Ni₃S₂ heteronanoflake arrays for highly enhanced electrochemical overall-water-splitting activity, *Nano Energy*, 2018, **51**, 26.

29 Y. Wu, G.-D. Li, Y. Liu, L. Yang, X. Lian, T. Asefa and X. Zou, Overall Water Splitting Catalyzed Efficiently by an Ultrathin Nanosheet-Built, Hollow Ni₃S₂-Based Electrocatalyst, *Adv. Funct. Mater.*, 2016, **26**, 4839.

30 T. Ling, D.-Y. Yan, H. Wang, Y. Jiao, Z. Hu, Y. Zheng, L. Zheng, J. Mao, H. Liu, X.-W. Du, M. Jaroniec and S.-Z. Qiao, Activating cobalt(II) oxide nanorods for efficient electrocatalysis by strain engineering, *Nat. Commun.*, 2017, **8**, 1509.

31 N. Singh, M. Gordon, H. Metiu and E. McFarland, Doped rhodium sulfide and thiospinels hydrogen evolution and oxidation electrocatalysts in strong acid electrolytes, *J. Appl. Electrochem.*, 2016, **46**, 497.

32 C. Hu, Y. Hu, C. Fan, L. Yang, Y. Zhang, H. Li and W. Xie, Surface-Enhanced Raman Spectroscopic Evidence of Key Intermediate Species and Role of NiFe Dual-Catalytic

Center in Water Oxidation, *Angew. Chem., Int. Ed.*, 2021, **60**, 19774.

33 N. Singh, J. Hiller, H. Metiu and E. McFarland, Investigation of the Electrocatalytic Activity of Rhodium Sulfide for Hydrogen Evolution and Hydrogen Oxidation, *Electrochim. Acta*, 2014, **145**, 224.

34 C. Yang, Z. Wang, T. Lin, H. Yin, X. Lu, D. Wan, T. Xu, C. Zheng, J. Lin, F. Huang, X. Xie and M. Jiang, Core-Shell Nanostructured "Black" Rutile Titania as Excellent Catalyst for Hydrogen Production Enhanced by Sulfur Doping, *J. Am. Chem. Soc.*, 2013, **135**, 17831.

35 D. Khang Ngoc, P. Zheng, Z. Dai, Y. Zhang, R. Dangol, Y. Zheng, B. Li, Y. Zong and Q. Yan, Ultrathin Porous NiFeV Ternary Layer Hydroxide Nanosheets as a Highly Efficient Bifunctional Electrocatalyst for Overall Water Splitting, *Small*, 2018, **14**, 1703257.

36 G. Ma, Q. Xue, J. Zhu, X. Zhang, X. Wang, H. Yao, G. Zhou and Y. Chen, Ultrafine Rh nanocrystals decorated ultrathin NiO nanosheets for urea electro-oxidation, *Appl. Catal., B*, 2020, **265**, 118567.

37 X. Meng, C. Ma, L. Jiang, R. Si, X. Meng, Y. Tu, L. Yu, X. Bao and D. Deng, Distance Synergy of MoS₂-Confined Rhodium Atoms for Highly Efficient Hydrogen Evolution, *Angew. Chem., Int. Ed.*, 2020, **59**, 10502.

38 S. Anantharaj, S. R. Ede, K. Karthick, S. S. Sankar, K. Sangeetha, P. E. Karthik and S. Kundu, Precision and correctness in the evaluation of electrocatalytic water splitting: revisiting activity parameters with a critical assessment, *Energy Environ. Sci.*, 2018, **11**, 744.

39 M. W. Louie and A. T. Bell, An Investigation of Thin-Film Ni-Fe Oxide Catalysts for the Electrochemical Evolution of Oxygen, *J. Am. Chem. Soc.*, 2013, **135**, 12329.

40 S. Lee, K. Banjac, M. Lingenfelder and X. Hu, Oxygen Isotope Labeling Experiments Reveal Different Reaction Sites for the Oxygen Evolution Reaction on Nickel and Nickel Iron Oxides, *Angew. Chem., Int. Ed.*, 2019, **58**, 10295.

41 S. Shi and D. Qin, Bifunctional Metal Nanocrystals for Catalyzing and Reporting on Chemical Reactions, *Angew. Chem., Int. Ed.*, 2020, **59**, 3782.

42 I. C. Man, H.-Y. Su, F. Calle-Vallejo, H. A. Hansen, J. I. Martinez, N. G. Inoglu, J. Kitchin, T. F. Jaramillo, J. K. Norskov and J. Rossmeisl, Universality in Oxygen Evolution Electrocatalysis on Oxide Surfaces, *ChemCatChem*, 2011, **3**, 1159.

43 F. Dionigi, Z. Zeng, I. Sinev, T. Merzdorf, S. Deshpande, M. B. Lopez, S. Kunze, I. Zegkinoglou, H. Sarodnik, D. Fan, A. Bergmann, J. Drnec, J. F. de Araujo, M. Gliech, D. Teschner, J. Zhu, W.-X. Li, J. Greeley, B. Roldan Cuenya and P. Strasser, *In situ* structure and catalytic mechanism of NiFe and CoFe layered double hydroxides during oxygen evolution, *Nat. Commun.*, 2020, **11**, 2522.

44 P. Zhang, H. Xiang, L. Tao, H. Dong, Y. Zhou, T. S. Hu, X. Chen, S. Liu, S. Wang and S. Garaj, Chemically activated MoS₂ for efficient hydrogen production, *Nano Energy*, 2019, **57**, 535.

45 W. Zhang, X. Zhang, L. Chen, J. Dai, Y. Ding, L. Ji, J. Zhao, M. Yan, F. Yang, C.-R. Chang and S. Guo, Single-Walled Carbon Nanotube Induced Optimized Electron Polarization of Rhodium Nanocrystals To Develop an Interface Catalyst for Highly Efficient Electrocatalysis, *ACS Catal.*, 2018, **8**, 8092.

46 B. Lu, L. Guo, F. Wu, Y. Peng, J. E. Lu, T. J. Smart, N. Wang, Y. Z. Finfrock, D. Morris, P. Zhang, N. Li, P. Gao, Y. Ping and S. Chen, Ruthenium atomically dispersed in carbon outperforms platinum toward hydrogen evolution in alkaline media, *Nat. Commun.*, 2019, **10**, 631.

47 Y. Xu, Y. Fo, H. Lv, X. Cui, G. Liu, X. Zhou and L. Jiang, Anderson-Type Polyoxometalate-Assisted Synthesis of Defect-Rich Doped 1T/2H-MoSe₂ Nanosheets for Efficient Seawater Splitting and Mg/Seawater Batteries, *ACS Appl. Mater. Interfaces*, 2022, **14**, 10246.

48 J. Yu, G. Li, H. Liu, L. Zhao, A. Wang, Z. Liu, H. Li, H. Liu, Y. Hu and W. Zhou, Ru-Ru₂P Phi NPC and NPC@RuO₂ Synthesized via Environment-Friendly and Solid-Phase Phosphating Process by Saccharomyces as N/P Sources and Carbon Template for Overall Water Splitting in Acid Electrolyte, *Adv. Funct. Mater.*, 2019, **29**, 1901154.

49 G. Chen, T. Wang, J. Zhang, P. Liu, H. Sun, X. Zhuang, M. Chen and X. Feng, Accelerated Hydrogen Evolution Kinetics on NiFe-Layered Double Hydroxide Electrocatalysts by Tailoring Water Dissociation Active Sites, *Adv. Mater.*, 2018, **30**, 1706279.

50 B. Ye, L. Huang, Y. Hou, R. Jiang, L. Sun, Z. Yu, B. Zhang, Y. Huang and Y. Zhang, Pt (111) quantum dot decorated flower-like Fe₂O₃ (104) thin film nanosheets as a highly efficient bifunctional electrocatalyst for overall water splitting, *J. Mater. Chem. A*, 2019, **7**, 11379.

51 K. Zhu, J. Chen, W. Wang, J. Liao, J. Dong, M. O. L. Chee, N. Wang, P. Dong, P. M. Ajayan, S. Gao, J. Shen and M. Ye, Etching-Doping Sedimentation Equilibrium Strategy: Accelerating Kinetics on Hollow Rh-Doped CoFe-Layered Double Hydroxides for Water Splitting, *Adv. Funct. Mater.*, 2020, **30**, 2003556.

52 B. H. R. Suryanto, Y. Wang, R. K. Hocking, W. Adamson and C. Zhao, Overall electrochemical splitting of water at the heterogeneous interface of nickel and iron oxide, *Nat. Commun.*, 2019, **10**, 5599.

53 X. Zhong, J. Tang, J. Wang, M. Shao, J. Chai, S. Wang, M. Yang, Y. Yang, N. Wang, S. Wang, B. Xu and H. Pan, 3D heterostructured pure and N-Doped Ni₃S₂/VS₂ nanosheets for high efficient overall water splitting, *Electrochim. Acta*, 2018, **269**, 55.

54 M. Zhao, W. Li, J. Li, W. Hu and C. M. Li, Strong Electronic Interaction Enhanced Electrocatalysis of Metal Sulfide Clusters Embedded Metal-Organic Framework Ultrathin Nanosheets toward Highly Efficient Overall Water Splitting, *Adv. Sci.*, 2020, **7**, 2001965.

55 M. Zhao, H. Li, W. Li, J. Li, L. Yi, W. Hu and C. M. Li, Ru-Doping Enhanced Electrocatalysis of Metal-Organic Framework Nanosheets toward Overall Water Splitting, *Chem. – Eur. J.*, 2020, **26**, 17091.

56 P. Chen, T. Zhou, M. Zhang, Y. Tong, C. Zhong, N. Zhang, L. Zhang, C. Wu and Y. Xie, 3D Nitrogen-Anion-Decorated Nickel Sulfides for Highly Efficient Overall Water Splitting, *Adv. Mater.*, 2017, **29**, 1701584.

57 L. Yu, H. Zhou, J. Sun, F. Qin, F. Yu, J. Bao, Y. Yu, S. Chen and Z. Ren, Cu nanowires shelled with NiFe layered double hydroxide nanosheets as bifunctional electrocatalysts for overall water splitting, *Energy Environ. Sci.*, 2017, **10**, 1820.

58 J. Luo, J.-H. Im, M. T. Mayer, M. Schreier, M. K. Nazeeruddin, N.-G. Park, S. D. Tilley, H. J. Fan and M. Graetzel, Water photolysis at 12.3% efficiency via perovskite photovoltaics and Earth-abundant catalysts, *Science*, 2014, **345**, 1593.

59 G. Zhang, Y.-S. Feng, W.-T. Lu, D. He, C.-Y. Wang, Y.-K. Li, X.-Y. Wang and F.-F. Cao, Enhanced Catalysis of Electrochemical Overall Water Splitting in Alkaline Media by Fe Doping in Ni_3S_2 Nanosheet Arrays, *ACS Catal.*, 2018, **8**, 5431.

60 Q. Wang, M. Ming, S. Niu, Y. Zhang, G. Fan and J.-S. Hu, Scalable Solid-State Synthesis of Highly Dispersed Uncapped Metal (Rh, Ru, Ir) Nanoparticles for Efficient Hydrogen Evolution, *Adv. Energy Mater.*, 2018, **8**, 1801698.

61 Y. Song, J. Cheng, J. Liu, Q. Ye, X. Gao, J. Lu and Y. Cheng, Modulating electronic structure of cobalt phosphide porous nanofiber by ruthenium and nickel dual doping for highly-efficiency overall water splitting at high current density, *Appl. Catal., B*, 2021, **298**, 120488.

62 D. Chen, Z. Pu, R. Lu, P. Ji, P. Wang, J. Zhu, C. Lin, H.-W. Li, X. Zhou, Z. Hu, F. Xia, J. Wu and S. Mu, Ultralow Ru Loading Transition Metal Phosphides as High-Efficient Bifunctional Electrocatalyst for a Solar-to-Hydrogen Generation System, *Adv. Energy Mater.*, 2020, **10**, 2000814.

63 J. Wang, F. Xu, H. Jin, Y. Chen and Y. Wang, Non-Noble Metal-based Carbon Composites in Hydrogen Evolution Reaction: Fundamentals to Applications, *Adv. Mater.*, 2017, **29**, 1605838.